Dynamics of the Holloway Current, the long-shore current on the Australian North West Shelf

K. Katsumata[1]and K. Ridgway[2]

[1]RIGC, JAMSTEC
[2]Oceans and Atmosphere, CSIRO

Key Points:

- Model simulation shows that the longshore current on Australia's North West Shelf flows SWward from Mar to Oct and reverses from Dec to Feb.
- The dynamics are geostrophic where not only seasonal winds and air-sea flux but waves and synoptic weather events form the pressure field.
- A coastal pressure maximum in Apr forms by coastally trapped wave passage with a contribution from local heating enhanced by tidal mixing.

Corresponding author: K. Katsumata, k.katsumata@jamstec.go.jp

Abstract

Observations and simulations have shown a coastally trapped current along the Australia North West Shelf, the Holloway Current. Using output from an ocean general circulation model with parameterized tidal mixing, we investigate the seasonal variation and driving mechanism of the Holloway Current. A budget analysis shows that in 2008 the current flows southwestward from March to October, is almost stagnant in November, and flows northeastward in January and February. At seasonal times scales, the Holloway Current is generally geostrophic. The pressure field is formed in summer, by a large scale pressure field augmented with the passage of coastally trapped waves from the Gulf of Carpentaria; in autumn, by the passage of the coastally trapped wave from the Gulf; and in winter/spring, by the large scale distribution of sea surface height. The acceleration mechanisms of the Holloway Current are in summer, the long-shore wind stress and the Coriolis force; in autumn/winter, the long-shore wind stress and the Coriolis force by the offshore current; and in spring, the pressure field working against the wind stress. The heat budget shows the near-shore high pressure in autumn is a result of water convergence after the passage of the coastally trapped wave with a secondary contribution from local atmospheric heating. Although the seasonal time scale is emphasized, the variation of the flow is strongest at daily to weekly time scales. The seasonal variability is a combination of seasonally varying large scale pressure field and the residual of these synoptic daily variability such as cyclones.

Plain Language Summary

The water masses and currents on the Australia North West Shelf are complicated; waters from the Pacific and Indian Oceans exist with modification by vigorous tides and seasonally reversing monsoon winds. Past observation and simulation identified a coherent ocean current along the coast flowing southwestward in autumn. We investigated the behavior and driving mechanism of this current, now referred to as the Holloway Current. The Holloway Current flows southwestward from March to October, almost stagnant in November, and flows northeastward in January and February. The flow is accelerated by the wind stress from summer to winter with the Coriolis force associated with onshore and offshore components of the flow. It is accelerated by the pressure gradient of the surrounding oceans in autumn, when it is flowing against the prevailing wind. The large scale, seasonal balance is between the pressure and the Coriolis force, where the pressure field is formed not only from seasonal atmospheric heating, evaporation and precipitation, but daily forcing such as cyclones and the passage of fast oceanic waves from the Gulf of Carpentaria.

1 Introduction

The Australia North West Shelf is characterized by strong tides – both external (Holloway, 1983) and internal (Holloway, 1984) – and offshore currents of both Pacific (Indonesian Throughflow, e.g. Godfrey (1996)) and Indian (Eastern Gyral Current, e.g. Menezes et al. (2013)) origin. It is known as the only subtropical eastern ocean boundary that does not show reduced temperatures near the coast under summer upwelling winds – an effect of the Pacific inflow

The circulation on the shelf has been described by climatological data (Gentilli, 1972; Godfrey & Mansbridge, 2000), sparse mooring observations (Holloway & Nye, 1985; Kronborg, 2004; Lowe et al., 2012; Maxime & Ming, 2019), and numerical simulation (Schiller, 2011; Maxime & Ming, 2019). The description is centered around a long-shore current, which varies seasonally. With mooring data from Jan 1982 to July 1983, Holloway and Nye (1985) demonstrated the existence of a seasonally varying southwestward flow with a maximum in autumn (April, May, June) and a reversal in summer (November, December, January, February). Holloway and Nye (1985) reported that the along-slope com-

ponent observed at a station (116°E, 19.5°S) with a water depth of 123 m shows a vertical mode-one-like structure with a peak at about 50 m depth for most of the time. They also examined the forcing by local wind and concluded that the wind is too weak to explain the observed flow and that the long-shore pressure gradient must drive the current. Indeed, their data show the current flowing against the prevailing wind in February – a situation reminiscent of the Leeuwin Current proper. Holloway and Nye (1985) (and later in Holloway (1995)) identified the long-shore current as an "extension of the Leeuwin Current". In this paper, we choose to follow D'Adamo et al. (2009) and Schiller (2011) referring to this this current as the Holloway Current.

Godfrey and Mansbridge (2000) were motivated by a qualitative description of surface currents of the region by Gentilli (1972) in attempting to close the volume and heat budget of the shelf circulation using climatological data. A number of assumptions and limited data prevented consistent budget calculations but both volume and heat budgets are not inconsistent with a southwestward flowing Holloway Current. Kronborg (2004), who referred to the Holloway Current as the extended Leeuwin Current, expanded the description by adding altimetry and mooring data to come up with further questions, such as identifying the role of the April sea level maximum in the seasonal forcing of the Holloway Current.

The seasonality of the Holloway Current is further documented using satellite altimetry, sea surface temperature, and an atmospheric reanalysis (Ridgway & Godfrey, 2015). It was shown that the onset of the long-shore current is triggered by a topographic Rossby wave modified by shelf friction whose origin can be traced all the way to Gulf of Carpentaria. Furthermore, they found that local atmospheric heat input around the Pilbara Shelf (between 17°S and 22°S) adds further sea surface height signal and contributes to the April maximum of the local sea surface height. They also verified results of Godfrey and Mansbridge (2000) that vigorous tidal mixing homogenizes the water column and promotes heat absorption at the surface.

The observations and simulation thus agree that the Holloway Current flows southwestward in autumn, in geostrophic balance with the near-shore pressure maximum. The flow description in other seasons varies but many observations indicate that flow reversals are often present (e.g. Holloway & Nye, 1985; Cresswell et al., 1993; Brink et al., 2007). In this paper, we attempt a more quantitative description of the Holloway Current throughout a complete year. Our domain of study is a broad shelf where water masses from the Pacific, Gulf of Carpentaria, and north east Indian Ocean meet under the seasonal reversal of the monsoon and the presence of vigorous tidal mixing. For good reason Godfrey and Mansbridge (2000) described it as an "oceanographically difficult region". Hence we turn to the output from a realistic simulation model for the quantitative analysis. Our main question is its dynamics – what drives the Holloway Current. The temporal resolution of the model allows the role of variability at the time scale of days to be taken in to consideration. We also diagnose the heat budget in a closed box to answer the question posed by Kronborg (2004) and Ridgway and Godfrey (2015); what is the role of local heat forcing in building up the pressure gradient in autumn?

2 Ocean General Circulation Model

The Ocean Forecast Australia Model (OFAM) (Oke et al., 2013) is based on version 4.0 of the Modular Ocean Model (Griffies et al., 2004). The spatial resolution is 0.1° in the Asia and Australia region (90−180°E, 75°S−16°N) which stretches to 2° in the North Atlantic. The vertical layer is 51 with a minimum resolution of 5 m near the surface. The model surface flux is given by ERA-40 reanalysis (Uppala et al., 2005) with the wind stress substituted by that from ERA-Interim (Dee et al., 2011). Enhanced mixing by internal and external tides are incorporated by parameterizing the output from a tidal prediction model (Oke et al., 2013). The model reproduces major features and

Figure 1. Annual average of surface velocity (arrows) and sea surface height (color). The arrows are shown every 0.8 degrees lon/lat. The rectangles NWSE and N'W'S'E' show the boxes for the budget analysis. The southwestward flowing current along the coast is the Holloway Current.

a number of metrics of the world ocean circulation (Oke et al., 2013), seasonal variation of the sea surface height in the region (Ridgway & Godfrey, 2015), and horizontal velocity field as observed by moorings on the shelf (Maxime & Ming, 2019). We choose 2008 to explore the circulation within this region. The first quarter of the year includes a La Nina event and is expected to show an enhanced Holloway Current (Schiller, 2011) and Indonesian Throughflow (Meyers, 1996), raising the signal-to-noise ratio of the dynamic analysis. Following the approach taken by (Godfrey & Mansbridge, 2000), we diagnose the budget of volume, heat, and momentum in a box shown in Fig.1. The offshore boundary of the box roughly corresponds to the shelf break at 200 to 400 m depth.

Figure 2. Bottom topography (color) and annual average wind stress (black arrows). The broken rectangle shows the box NWSE in Fig.1.

3 Dynamics of the Holloway Current

3.1 Annual Average

Before studying the time varying components of the circulation, we discuss the annual averaged circulation (Figs.1 and 2). The annual average surface flow (Fig.1) clearly shows the Holloway Current as a long-shore southwestward flowing current which continues to flow around the North West Cape to join the Leeuwin Current proper (Lowe et al., 2012). The surface flow approximately follows the isoline of the sea surface height, a proxy for the pressure field, with high pressure on the left-hand side looking downstream, suggesting that the flow is in the geostrophic balance. Under geostrophy, a sea level difference of 3 cm across a 100 km wide current is balanced by a flow of 0.1 ms^{-1}, giving the right order of magnitude (Fig.1).

The core of the Holloway Current is found on the shelf with depths less than 200 m (Fig.2). The depth contours are almost parallel to the geostrophic contours (f/H =constant, not shown) and do not extend offshore. This implies that there is no inviscid commu-

nication of the offshore dynamics and the Holloway Current driven by Rossby waves, a mechanism which has been found to be essential in the trapping of the Leeuwin Current along the boundary to the south of North West Cape (Furue et al., 2013).

The wind varies seasonally with a maximum amplitude of about 0.3 Nm^{-2}, but the oscillating component in the long-shore direction cancels out and the annual average wind is offshore (Fig.2). The offshore wind stress of τ =0.03 Nm^{-2} carries 1 $\mathrm{m}^2\mathrm{s}^{-1}$ ($= \tau/(f\rho)$) of Ekman transport, which is roughly 0.1 Sv of the long-shore transport in a 100 km wide current. This is approximately one third of the annual average Holloway Current transport (see later Fig.3).

The annual average component of the Holloway Current is thus explained by the geostrophic balance augmented by Ekman transport. Both the pressure gradient and wind stress are in the offshore direction.

3.2 Seasonal Variation

In order to examine the seasonal variation, the daily time series of transports across three boundaries of the analysis box NWSE (Fig.1) are integrated in time such that seasonal rather than daily time scales are emphasized and that accumulated transport can be quantified (Figure 3). Unfortunately the volume budget does not close, due to interpolation errors related to coordinate rotations. However, Fig.3 shows that the error is smaller than each of the three components. The variability shown in Fig.3 suggests three flow patterns; November to February (which we call "summer") – inflow from the NW and outflow from the NE, March to June ("autumn") – inflow from the NE and outflow from both the NW and the SW; and July to October ("winter/spring") – inflow from the NE and outflow from the SW. We note that these periods do not correspond directly to the monsoon seasons – onshore northwesterly in January and February and offshore southeasterly from May to August. This is consistent with the discussion by Holloway and Nye (1985) that the Holloway Current is not solely wind driven. The flow through the NW boundary shows vertically integrated cross-shore transport. The onshore monsoon has a northeastward component such that is upwelling favourable with onshore total transport, opposing the offshore surface Ekman transport. We note the onshore geostrophic transport is not a direct response to the monsoon, but supported by long-shore pressure gradient (subsection 3.5). In contrast, the downwelling monsoon from May to August is associated with the offshore vertically-integrated transport. The NW transport shows a very weak semiannual signal. This signal and intraseasonal variabilities (period 30 to 90 days) have been discussed in detail by Maxime and Ming (2019).

The annual average Holloway Current transport as evaluated through the SW boundary is approximately 0.3 Sv ($= -10 \times 10^{12}$ m^3 / year). The southwestward transport through the NE boundary is about 60 % larger, which is balanced by the offshore transport through the NW boundary from March to August.

In summer (November to February; Fig.4a), the flow across the NW is onshelf, as expected from the high sea surface "tongue" along 12°S, northeast of the boundary. The origin of this "tongue" is discussed later in subsection 3.5. On the other hand, the flow across the NE is towards the northeast despite the presence of a rather flat pressure field. In fact, this northeastward flow near the NE boundary is a response to daily to weekly enhancement of the northeastward wind stress and thus is not in geostrophic balance. Such ageostrophic components are observed when the wind is strong (January, February, May, and June) and will be discussed under the daily variability section 3.4.

In autumn (March to June; Fig.4b), the Holloway Current is strongest and not only in approximate geostrophic balance but also augmented by an Ekman transport contribution driven by the offshore monsoon wind in May and June. Ridgway and Godfrey (2015) demonstrated with satellite altimetry that this along-shore high pressure occurs

Figure 3. Transports across three boundaries of the box NWSE shown in Figs.1 and 2. The daily transport is integrated in time such that an increase in the integrated transport means positive transport across the boundary. Positive in the long-shelf and cross-shelf direction are towards northeast and northwest, respectively. Due to the coordinate rotation, the transports do not balance where NE−SW+NW indicates the magnitude of the imbalance. Ticks in the horizontal axis are placed on the first day of the month.

Figure 4. Three flow regimes identified from the seasonal variation of transports (Fig.3). Sea surface height (color) and horizontal flow averaged over upper 95m (arrows) are shown after temporarily averaging over the three periods. The broken line show the box NWSE. Monthly averaged wind stress vectors spatially averaged within the box are shown near the bottom on land with the white circles showing a scale for 0.05 Nm^{-2}.

in this season after the passage of a wave front propagating from the Gulf of Carpentaria where the southeastward blowing monsoon wind in summer builds up high sea level. The sea level signal propagates anticlockwise around Australia and is strongest in March to May on the North West Shelf. The dynamics of the along-shore high pressure will be examined in detail in section 4.

In winter/spring (July to October; Fig.4c), the Holloway Current is weaker and the pressure field indicated by the sea surface height does not appear to support geostrophy, particularly in the northeastern half of the box. We further investigate the momentum balance to clarify the driving mechanism of this weak Holloway Current.

3.3 Long-shelf momentum balance

The momentum equation in the long-shelf direction, x, is

$$\frac{\partial}{\partial t}\int_{-H}^{\eta}\rho u\mathrm{d}z = -\int_{-H}^{\eta}\frac{\partial p}{\partial x}\mathrm{d}z + \int_{-H}^{\eta}\rho f v\mathrm{d}z + \tau_x + \text{adv.} + \text{dis.}, \tag{1}$$

where ρ is density, η is sea surface height, $-H$ is depth, u is the long-shelf velocity (positive northeast), v is cross-shelf velocity (positive northwest), τ_x is wind stress in x direction and the last 2 terms on the right hand side are advection and dissipation, respectively. The balance is integrated in the analysis box NWSE (Fig.5). The primary balance of the long-shelf momentum is among the Coriolis, pressure gradient, and wind stress term. The small size of the advection term suggests that in this region the system is controlled by linear dynamics. This is in contrast to the mid-latitude west coast of Australia, where Feng et al. (2005) found that the nonlinear term expressed as eddy Reynolds stress to drive the Leeuwin Current ($\sim 30°$S) is comparable to the pressure gradient and wind stress. The eddy kinetic energy on the North West Shelf is much weaker than the eddies there (less than quarter, figure not shown) and hence we expect the nonlinear term is negligible here.

Following the cessation of the offshore monsoon in September, the wind stress remains positive until March, decelerating the southwestward flow of the Holloway Current (Fig.5). It is during this period that previous observations have shown the Holloway Current flowing directly into the wind (Cresswell et al., 1993). To overcome the wind stress forcing, the required poleward acceleration is provided by a negative long-shore pressure gradient (Fig.5). Between March and November, the Coriolis force associated with the offshore current accelerates the Holloway Current. Both the Holloway Current and the onshore flow switches around to the opposite direction in December. Thus we conclude that during September and October, the Holloway Current is accelerated directly into the wind by the components of the pressure gradient that is not balanced by the Coriolis force associated with the cross-shore current. The role of the large scale pressure field driving the Holloway Current was also noted by Godfrey and Mansbridge (2000). They found that the offshore long-shore steric height difference was in phase with the coastal sea level difference between Darwin and Carnarvon.

In summary, the momentum balance shown in Fig.5 suggests the following seasonal forcing of the Holloway Current. During autumn and winter (from March to August), the southwestward flowing Holloway Current is driven by the long-shore wind stress and the Coriolis force associated with the offshore current. During spring to summer (September to February), the large scale pressure field – higher northeastward – drives the Holloway Current. Wind stress works in the opposite direction. The Coriolis force is southwestward from March to December. These opposing forcings result in an almost stagnant Holloway Current in November (Fig.3). In December, the Holloway Current turns northeastward, in the same direction as the Coriolis force (associated with the cross-shore current) which also turns onshore in December in response to the onset of upwelling favourable winds.

Figure 5. Long-shelf momentum balance, Eq.(1). The terms are evaluated on the right hand side such that positive is to accelerate the momentum northeastward. The terms have been integrated in time. Light blue line is the Coriolis term, green is the pressure gradient, red is the wind stress, black is advection, and blue is the long-shore momentum. Dissipation was not calculated.

Figure 6. Daily time series of the long-shelf momentum balance (1). Only the pressure gradient term (green, right vertical axis), wind stress (red, right axis), and momentum (blue, left axis) are shown, integrated in the analysis box NWSE in Fig.1.

3.4 Short Time Scales, Daily to Weekly

We now examine the unintegrated time series of the long-shelf momentum balance (Fig.6). Note the dominance of daily to weekly time scales in the variations of the momentum terms (e.g. Lowe et al., 2012). The peaks in wind stress correspond well with the peaks in the momentum with the same sign, suggesting ageostrophic oceanic responses to the wind. This wind drag accumulates surface water and builds a pressure gradient that counteracts the wind stress, which is also seen in the anti-correlation between wind stress and long-shelf pressure gradient. A closer look shows that this quick response to wind holds well during autumn (May, June) to winter (July, August), as well as in summer (January, February). At these times, the monsoon winds are near their extremes; onshore in summer and offshore in autumn and winter. When the wind is in transition between the two monsoonal peaks, the anti-correlation between the wind stress and pressure gradient holds, but the momentum (i.e. Holloway Current) does not follow the wind. As seen in Fig.5, only the pressure gradient provides the forcing to the Holloway Cur-

rent in the right direction during this period. Hence we conclude that the Holloway Current is driven by the part of pressure gradient not balanced by the Coriolis force. During March and April, the high pressure signal from the Gulf of Carpentaria builds up an offshore pressure gradient (Ridgway & Godfrey, 2015) which leads to Coriolis acceleration of the momentum and the onset of southwestward flowing Holloway Current.

During summer (late November to February), the Holloway Current changes directions on weekly time scales. The flow reversals are also seen in June and July, agreeing with an observed reversal in July 2003 (Brink et al., 2007).

3.5 High Sea Level along 12°S in Summer

The inflow during summer from the NW boundary (Fig.3) is supported by the high pressure tongue along 12°S (Fig.4a). Since the westward flow of the South Equatorial Current (SEC) augmented by the Indonesian Throughflow is strongest at this latitude (Fig.1), the high sea level is partly explained by the advection of warm water originating from the equatorial region. However, this does not explain the seasonal variation of the tongue, which is weak in winter when the SEC is at its peak (Fig.4). We explore the temporal variation of sea level within a Hovmoller plot of the annual variation of the sea surface height along 12°S (Fig.7). The figure shows two distinct propagation features to the west and east of 120°E. The western feature is related to the monthly westward propagation of eddies with speeds between 0.15 to 0.19 ms^{-1}, generated from the shear instability of the Throughflow (Feng & Wijffels, 2002). In the east, a sequence of disturbances propagate westward at much higher frequency and speed from 125° to 143∘E (see the black dashed line).

In January and February when the SEC is weak, pulses of high ($>$ 1.0m) sea surface height propagate from the Gulf of Carpentaria (east of $\sim$ 135°E) at a much faster speed ($\approx$ 0.8 ms^{-1}) than the eddies. From several pulses found in January and February in Fig.7, the spatial evolution of one pulse at the end of February is illustrated in Fig.8. Sea surface builds up against the eastern boundary of the Gulf of Carpentaria up to 19th February in response to the southeastward blowing wind. The high sea surface height is released from the 20th to the 22nd and a wave is seen as the 0.70 m contour (between blue and light blue) to propagate as a coastal wave. Perhaps due to the westward advection by the SEC, the decaying wave shows a similar shape to the tongue on 23rd Feb.

The propagation speed of about 0.8 ms^{-1} is much slower than the 2 to 10 ms^{-1} propagation speed of coastally trapped waves found on the southern and eastern sides of Australia (Woodham et al., 2013). However, this is not an unlikely speed for coastally trapped waves given that the coast is not parallel to the latitudinal circle used in Fig.7 and that complicated shelf topography and friction can retard the propagation as pointed out by Ridgway and Godfrey (2015).

We thus conclude that the tongue is the average of these coastal wave pulses modified by the SEC and the Indonesian Throughflow. It is interesting that these pulses do not propagate further than 117°E when they are strong in January and February. In March and April, the pulses are weaker but they start the circum-Australia propagation reported in Ridgway and Godfrey (2015). The reason for this behavior is not known, but the weakening wind stress in March might be a contributing factor.

4 Heat Budget

In this section, we examine the role of surface heating on the Holloway Current dynamics. As already noted, the maximum poleward flow of the Holloway Current occurs in autumn when it is in geostrophic balance with the high pressure along the coast (Fig.4b).

Figure 7. Sea surface height along 12°S. The white dashed line shows a propagation at 0.18 ms^{-1}, while the black at 0.8 ms^{-1}.

Figure 8. Daily averages of sea surface height (color) and wind stress (arrows) from 17 Feb to 24.

Kronborg (2004) identified this pressure structure from satellite altimeter and emphasized the role of heat advection from the Arafura Sea. Previously Godfrey and Mansbridge (2000) discussed the heat budget on the shelf using limited climatological data, where it was speculated that the excess heat input from the atmosphere onto the shelf is exported by the onshelf transport of deep cold water balanced by export of warmer surface water. Ridgway and Godfrey (2015) demonstrated with the satellite altimeter that the high sea level along the coast in autumn can be traced back to Gulf of Carpentaria. They also noted that the time-distance plot of the sea level signal shows a kink near our analysis box NWSE and discussed the possible role of local atmospheric heating during summer months. All three studies emphasized the role of breaking internal tides in the rapid vertical redistribution of the surface heating.

We quantify the roles of advection and local atmospheric heating by examining the heat budget. In order to focus on the high sea level region, the budget analysis was performed in a smaller box N'W'E'W' in Fig.1. The heat content H within the box

$$\frac{\partial H}{\partial t} = -\frac{\partial}{\partial x}\int_{-H}^{\eta} Tu^2 \mathrm{d}z - \frac{\partial}{\partial y}\int_{-H}^{\eta} Tuv\mathrm{d}z + \frac{\mathcal{F}}{C\rho_0} + \mathcal{D}, \tag{2}$$

where H is internal energy ("heat"), T is temperature, $\mathcal{F}$ is surface heat flux from the atmosphere, $\mathcal{D}$ is dissipation, and heat capacity C was constant (=4003 J kg^{-1} °C) and evaluated at the mean surface temperature and salinity of 28.056°C and 34.49, respectively. Equation (2) is integrated within N'W'S'E' and also in time (Fig.9).

The time change in the heat content ΔH shows a seasonal variation with a maximum in April and a minimum in August. The variation follows that of the accumulated atmospheric flux. The advection always takes heat away from the region and does not sum up to zero, suggesting year-to-year variations. Although temperature transport through each boundaries is much larger than these terms (note temperature transport (NE, SW, NW) were scaled down in Fig.9a), their summation is of smaller contribution than the atmospheric flux.

The difference between the accumulated heat flux (red) and heat content change (blue) increases from January to April. This difference is partly balanced by the heat removal by advection. The difference decreases from September to November as the heat content increases. Given that the contribution of advection almost cancels out during this period it is not clear what reduces the difference. One candidate is horizontal heat diffusion, which was not included in the diagnosis calculation. Kronborg (2004) estimated the horizontal heat transport by eddies using high-pass filtered (with a threshold period of 135 days) time series of temperature and velocity from moorings located on the Arafura Sea (along the NE boundary of our analysis box, further northeast). The mooring data from August 1999 to September 2000 proved most active eddies during spring (September to November).

Towards the April maximum, the heat increase during March is $\Delta H \approx 10^{13}$°C·m^3. If this heat is distributed in the top D m, of the box (with area $A = 2.6 \times 10^{11}$m^2), this will increase the temperature by $\Delta H/(AD)$ With an approximate thermal expansion ($\alpha = -(\partial\rho/\partial T)/\rho$) of $\alpha = 0.3 \times 10^{-3}$(°C^{-1}), density in the top D m decreases by an ratio $\alpha\Delta H/(AD)$. As a result, under this approximation of constant α, the sea level increases by $\alpha\Delta H/A \approx 0.012$m regardless of D. From March to April, the sea surface in this region increases approximately 0.1 m (see Fig.4). This back-of-envelope calculation shows that although the contribution of local heating is substantial in the heat budget, its contribution to sea level is an order smaller than the total sea level rise, which is mainly due to the wave propagation and concurrent flow convergence in April. The flow convergence includes the contribution of onshore Ekman transport.

Figure 9. (a) Energy balance Eq.(2) and (b) volume budget in the box N'W'S'E' (Fig.1). In (a), surface flux from the atmosphere (red), advection (purple), and heat content change from 1st January (blue) are shown in the unit of °C m^3, i.e. the flux and advection have been integrated in time. Three components of advection are shown by thin solid lines (green, light blue, and orange) with magnitudes diminished by a factor of 5. For advection of "heat" (Warren, 1999), northeastward is positive for NE and SW, and northwestward is positive for NW. Before evaluating (2), a uniform correction to flow speed is added such that the volume conserves, i.e. $U_{NE} + V_{NW} - U_{SW} = 0$ (see purple line in (b)). The correction was calculated daily with a root mean square value of $1.2 \times 10^3 \mathrm{ms}^{-1}$.

Figure 10. Daily averaged heat flux (color, positive into the ocean) and wind stress (arrows) from 7th February 2008 to 17th. The cyclonic wind conspicuous on 15th Feb is Severe Tropical Cyclone Nicholas.

4.1 Tropical Cyclone Nicholas

Both the heat content and accumulated surface flux shows a dip in mid-February. The dip can also be seen in accumulated (Fig.5) and daily (Fig.6) wind stress. These are caused by Tropical Cyclone Nicholas (Fig.10). The tropical cyclone Nicholas showed a peak intensity of 948 hPa with a maximum gust of 59 ms^{-1} (Paterson, 2008). Since the arrival of Nicholas followed a relatively quiet period, it has a prominent effect on the momentum and heat budgets. The strong surface flow in Fig.4a near 15°S, 125°E was also caused by the ageostrophic responses to the cyclone.

5 Discussion

5.1 Interannual variability

In this study we have built a description of the behavior of the Holloway Current from model output for a single year, 2008. Does this single year provide a representative picture of the regional circulation, particularly at seasonal time scales? More specifically, is the magnitude of interannual variability of the system great enough to neutralize the strong seasonality observed in our study? In fact, there are many observations that support the dominance of seasonal peaks in autumn, however, when the flow is relatively weak, some interannual variability does exist. For example, D'Adamo et al. (2009) reported results from a six-year mooring, showing steady southwestward flow in autumns but with weak flow reversals from July to November.

In a multi-year simulation, Schiller (2011) found interannual variability in the Indonesian Throughflow (flow between the Timor Island and Australia). The Throughflow is approximately 8 Sv from the Pacific to the Indian Oceans with a seasonal variation of ± 2 Sv. On this seasonality, there is an additional interannual variability of around $\pm$ 2 Sv. A few extreme interannual peaks do exist with magnitude up to 4 Sv but these tend to enhance the underlying seasonal variability. The model result from 1994 to 2008 thus suggests that interannual variability does not mask the seasonal variability. Further observations, including a two year drifter survey by Cresswell et al. (1993) and a two year mooring deployment by Holloway and Nye (1985) also show dominance of seasonal over interannual variability under strong monsoons. We thus conclude that the seasonal variability reported in this paper holds in other years at least for strong monsoon periods from February to July.

5.2 What drives the Holloway Current?

This question is not sufficiently specific for a quantitative discussion. On one hand, a textbook scaling of the momentum equation shows that geostrophy is the dominant balance under seasonal time scales. In fact, on the North West Shelf, the ratio of the nonlinear advection term to the Coriolis term, the Rossby number, as evaluated with a length scale of 100 km and the maximum speed throughout the year at every grid point, is generally less than 0.3 and not exceeding 0.5 (figure not shown), suggesting that geostrophic balance applies. Geostrophy is also supported by observed data at spatial scales larger than 16 km and temporal scales of weekly or longer (Brink et al., 2007). However, geostrophy is just a balance and does not explain the acceleration mechanism of the flow, nor how the balance has been established. Figures 5 and 6 demonstrate that the long-shore wind stress τ_x contributes to the variability of the long-shore momentum ρu, i.e. the Holloway Current. This is not reflected in the geostrophic argument.

From the geostrophic view point, the question boils down to *what mechanism forms the pressure field*, as shown in Fig.4. In summer, it is the large scale pressure field augmented by the passage of coastally trapped waves from the Gulf of Carpentaria (section 3.5). In autumn, it is the passage of the coastally trapped wave from the Gulf of Carpentaria that leaves the conspicuous high pressure along the coast (Ridgway & Godfrey, 2015). In winter/spring, the pressure field seems to follow the large scale distribution of sea surface height. The wind stress contributes to the pressure field first by building up the large scale pressure field exemplified in Gulf of Carpentaria (Fig.10) and second by Ekman pumping exemplified by the winter monsoon with a southwestward component that contributes to the near-shore flow convergence in May and June. A close look at the panels in Fig.4 suggests, however, that the geostrophy does not seem to hold, particularly in the northeastern half of the box NWSE in winter/spring. In this stagnant period, the flow is more turbulent and transports by eddies (Kronborg, 2004) might play a role. Brink et al. (2007) found that meso- and submeso-scale eddies are important in the local energy balance, however, they are not fully resolved in the present simulation.

Another example of ageostrophic dynamics is the strong surface flow in Fig.4(a) near 15°S, 125°E associated with Cyclone Nicholas. The presence of this peaky flow means that applying a four month averaging filter is not sufficient to remove their influence (see Fig.4a).

From the momentum balance view point, the contribution of the Ekman transport is absorbed in the balance amongst the Coriolis, pressure, and wind stress terms. In the long-shore momentum equation, the geostrophic balance by the near-shore sea level maximum does not show up. An imbalance in the geostrophic balance of the cross-shore pressure and long-shore flow will cause a perturbation in the cross-shore flow, which in turn deflects by the Coriolis force and establishes a new geostrophic balance of the long-shore flow. The daily time series of long-shore momentum (Fig.5) shows that the wind stress is almost instantaneously balanced by pressure gradient but this counteraction does not completely cancel the wind stress and the small residual drives the Holloway Current. The difference in magnitude of the momentum change ($O(10^{15})$ kgms^{-1}, Fig.6) and forcing magnitude ($O(10^{16})$ kgms^{-1}, Fig.5) means that even with the budget calculation with daily averaged model output, it is difficult to examine the momentum balance quantitatively. Perhaps a more robust result can be obtained by discussing the sign of the forcing – if the direction of acceleration is consistent with the observed flow, the forcing may be considered to be "driving" the flow.

In this way, we conclude that the driving mechanisms of the seasonal Holloway Current are from March to August, the long-shore wind stress and the Coriolis force associated with the offshore current; from September to October, it is the pressure field working against the wind stress; and from December to February the long-shore wind stress and the Coriolis force.

Acknowledgments

This work is based on an unpublished manuscript by J.S.Godfrey. We thank Dr. Furue for his comments. The Bluelink ocean data product were provided by CSIRO and these data are publicly available on the National Compuatational Infrastructure server (https://dap.nci.org.au/thredds/ Bluelink is a collaboration involving the Commonwealth Bureau of Meteorology, the CSIRO, and the Royal Australian Navy.

References

Brink, K. H., Bahr, F., & Shearman, R. K. (2007). Alongshore currents and mesoscale variability near the shelf edge off northwestern australia. *Journal of Geophysical Research: Oceans*, *112*(C5). doi: 10.1029/2006JC003725

Cresswell, G., Frische, A., Peterson, J., & Quadfasel, D. (1993). Circulation in the timor sea. *Journal of Geophysical Research: Oceans*, *98*(C8), 14379–14389.

Dee, D. P., Uppala, S. M., Simmons, A. J., Berrisford, P., Poli, P., Kobayashi, S., ... others (2011). The era-interim reanalysis: Configuration and performance of the data assimilation system. *Quarterly Journal of the royal meteorological society*, *137*(656), 553–597.

D'Adamo, N., Fandry, C., Buchan, S., & Domingues, C. (2009). Northern sources of the leeuwin current and the "holloway current" on the north west shelf. *Journal of the Royal Society of Western Australia*, *92*, 53–66.

Feng, M., & Wijffels, S. (2002). Intraseasonal variability in the south equatorial current of the east indian ocean. *Journal of physical oceanography*, *32*(1), 265–277.

Feng, M., Wijffels, S., Godfrey, S., & Meyers, G. (2005). Do eddies play a role in the momentum balance of the leeuwin current? *Journal of Physical Oceanography*, *35*(6), 964-975. doi: 10.1175/JPO2730.1

Furue, R., McCreary, J. P., Benthuysen, J., Phillips, H. E., & Bindoff, N. L. (2013). Dynamics of the leeuwin current: Part 1. coastal flows in an inviscid, variable-

density, layer model. *Dynamics of Atmospheres and Oceans*, *63*, 24–59.

Gentilli, J. (1972). Thermal anomalies in the eastern indian ocean. *Nature Physical Science*, *238*(84), 93–95.

Godfrey, J. S. (1996). The effect of the indonesian throughflow on ocean circulation and heat exchange with the atmosphere: A review. *Journal of Geophysical Research: Oceans*, *101*(C5), 12217–12237.

Godfrey, J. S., & Mansbridge, J. V. (2000). Ekman transports, tidal mixing, and the control of temperature structure in australia's northwest waters. *Journal of Geophysical Research: Oceans*, *105*(C10), 24021–24044.

Griffies, S. M., Harrison, M. J., Pacanowski, R. C., & Rosati, A. (2004). A technical guide to mom4. *GFDL Ocean Group Tech. Rep*, *5*, 371.

Holloway, P. E. (1983). Tides on the australian north-west shelf. *Marine and Freshwater Research*, *34*(1), 213–230.

Holloway, P. E. (1984). On the semidiurnal internal tide at a shelf-break region on the australian north west shelf. *Journal of Physical Oceanography*, *14*(11), 1787-1799. doi: 10.1175/1520-0485(1984)014⟨1787:OTSITA⟩2.0.CO;2

Holloway, P. E. (1995). Leeuwin current observations on the australian north west shelf, may–june 1993. *Deep Sea Research Part I: Oceanographic Research Papers*, *42*(3), 285–305.

Holloway, P. E., & Nye, H. C. (1985). Leeuwin current and wind distributions on the southern part of the australian north west shelf between january 1982 and july 1983. *Marine and Freshwater Research*, *36*(2), 123–137.

Kronborg, M.-B. (2004). *Ocean circulation over the north west shelf of australia: Does it impact on the leeuwin current?* (Unpublished doctoral dissertation). Danish Center for Earth System Science, University of Copenhagen.

Lowe, R. J., Ivey, G. N., Brinkman, R. M., & Jones, N. L. (2012). Seasonal circulation and temperature variability near the north west cape of australia. *Journal of Geophysical Research: Oceans*, *117*(C4). doi: 10.1029/2011JC007653

Maxime, M., & Ming, F. (2019). Intra-annual variability of the north west shelf of australia and its impact on the holloway current: Excitement and propagation of coastally trapped waves. *Continental Shelf Research*, *186*, 88–103. doi: 10.1016/j.csr.2019.08.001

Menezes, V. V., Phillips, H. E., Schiller, A., Domingues, C. M., & Bindoff, N. L. (2013). Salinity dominance on the indian ocean eastern gyral current. *Geophysical Research Letters*, *40*(21), 5716-5721. doi: 10.1002/2013GL057887

Meyers, G. (1996). Variation of indonesian throughflow and the el niño-southern oscillation. *Journal of Geophysical Research: Oceans*, *101*(C5), 12255-12263. doi: 10.1029/95JC03729

Oke, P. R., Griffin, D., Schiller, A., Matear, R. J., Fiedler, R., Mansbridge, J., ... Ridgway, K. R. (2013). Evaluation of a near-global eddy-resolving ocean model. *Geosci.Model Develop*, *6*, 591–615. doi: 10.5194/gmd-6-591-2013

Paterson, L. (2008). Tropical Cyclone *Nicholas*. In *http://www.bom.gov.au/*. Australia Bureau of Meteorology. (Downloaded from `http://www.bom.gov.au/cyclone/history/nicholas.shtml` on 3 July 2020)

Ridgway, K. R., & Godfrey, J. S. (2015). The source of the leeuwin c urrent seasonality. *Journal of Geophysical Research: Oceans*, *120*(10), 6843–6864.

Schiller, A. (2011). Ocean circulation on the north australian shelf. *Continental Shelf Research*, *31*(10), 1087–1095.

Uppala, S. M., Kållberg, P. W., Simmons, A. J., Andrae, U., Bechtold, V. D. C., Fiorino, M., ... others (2005). The era-40 re-analysis. *Quarterly Journal of the Royal Meteorological Society: A journal of the atmospheric sciences, applied meteorology and physical oceanography*, *131*(612), 2961–3012.

Warren, B. A. (1999). Approximating the energy transport across oceanic sections. *Journal of Geophysical Research: Oceans*, *104*(C4), 7915-7919. doi: 10.1029/1998JC900089

Woodham, R., Brassington, G. B., Robertson, R., & Alves, O. (2013). Propagation characteristics of coastally trapped waves on the australian continental shelf. *Journal of Geophysical Research: Oceans*, *118*(9), 4461-4473. doi: 10.1002/jgrc.20317

Figure 1.

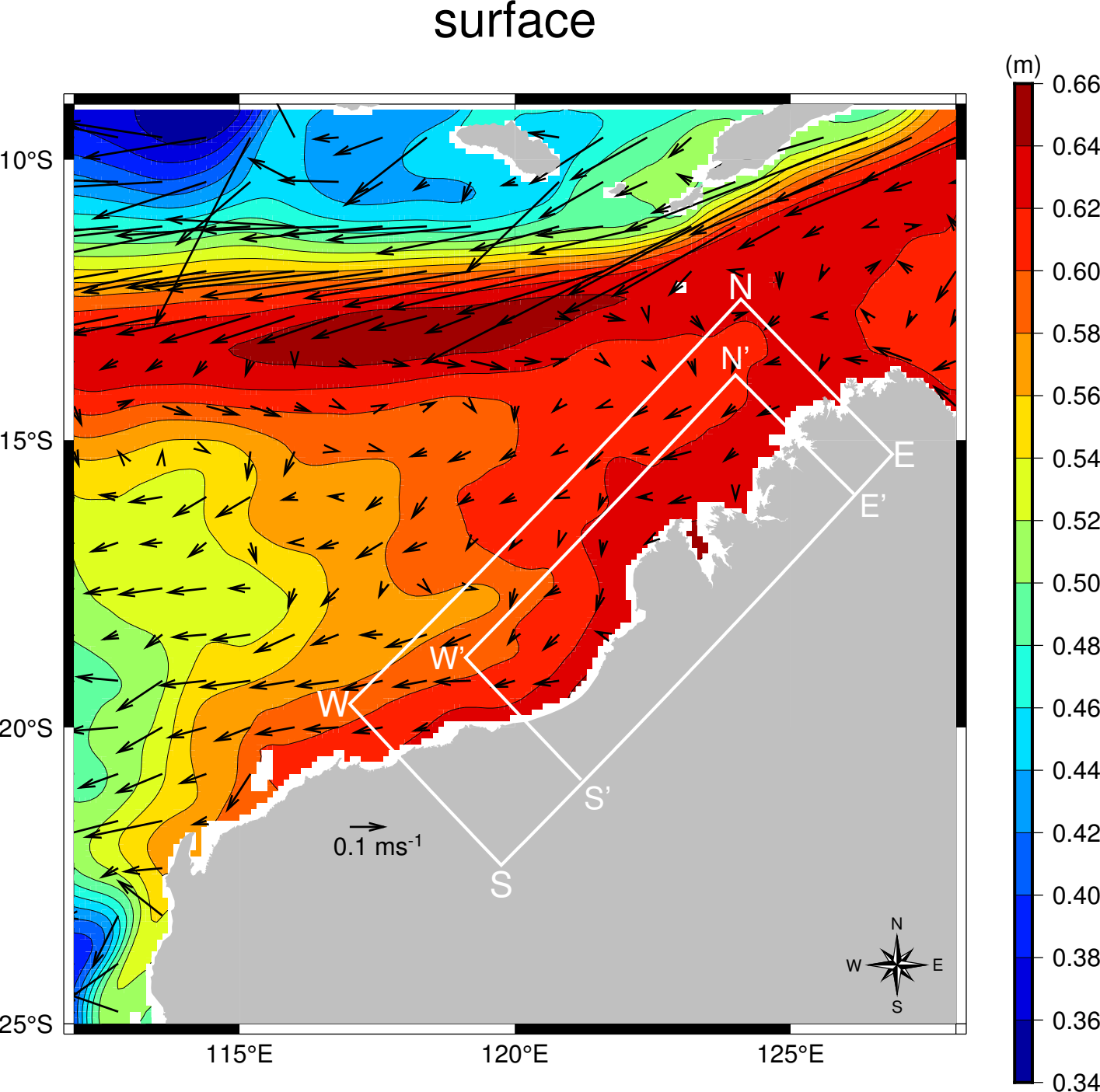
surface
(m)
0.66
0.64
0.62
0.60
0.58
0.56
0.54
0.52
0.50
0.48
0.46
0.44
0.42
0.40
0.38
0.36
0.34
10°S
15°S
20°S
25°S
115°E
120°E
125°E
N
N'
E
E'
W'
W
S'
S
0.1 ms-1
N
W
E
S

Figure 2.

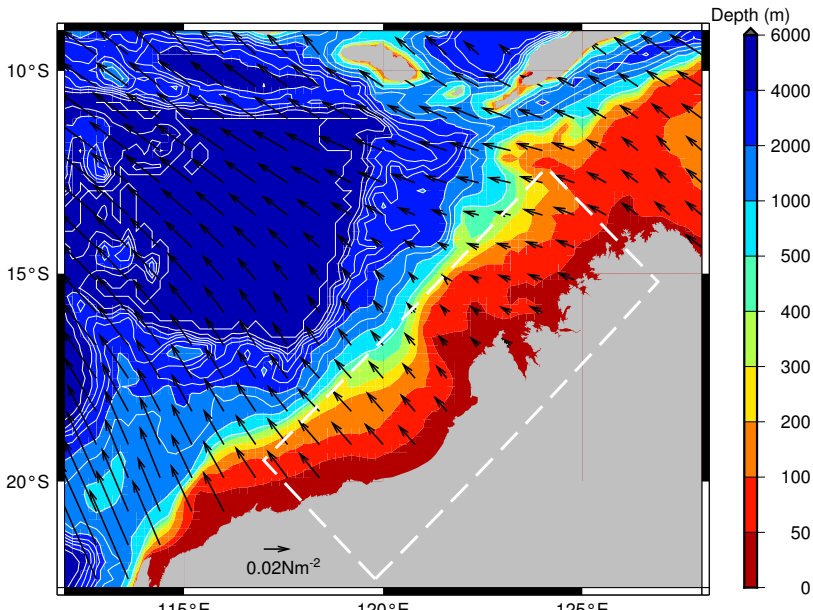
Depth (m)
6000
4000
2000
1000
500
400
300
200
100
50
0
10°S
15°S
20°S
115°E
120°E
125°E
0.02Nm-2

Figure 3.

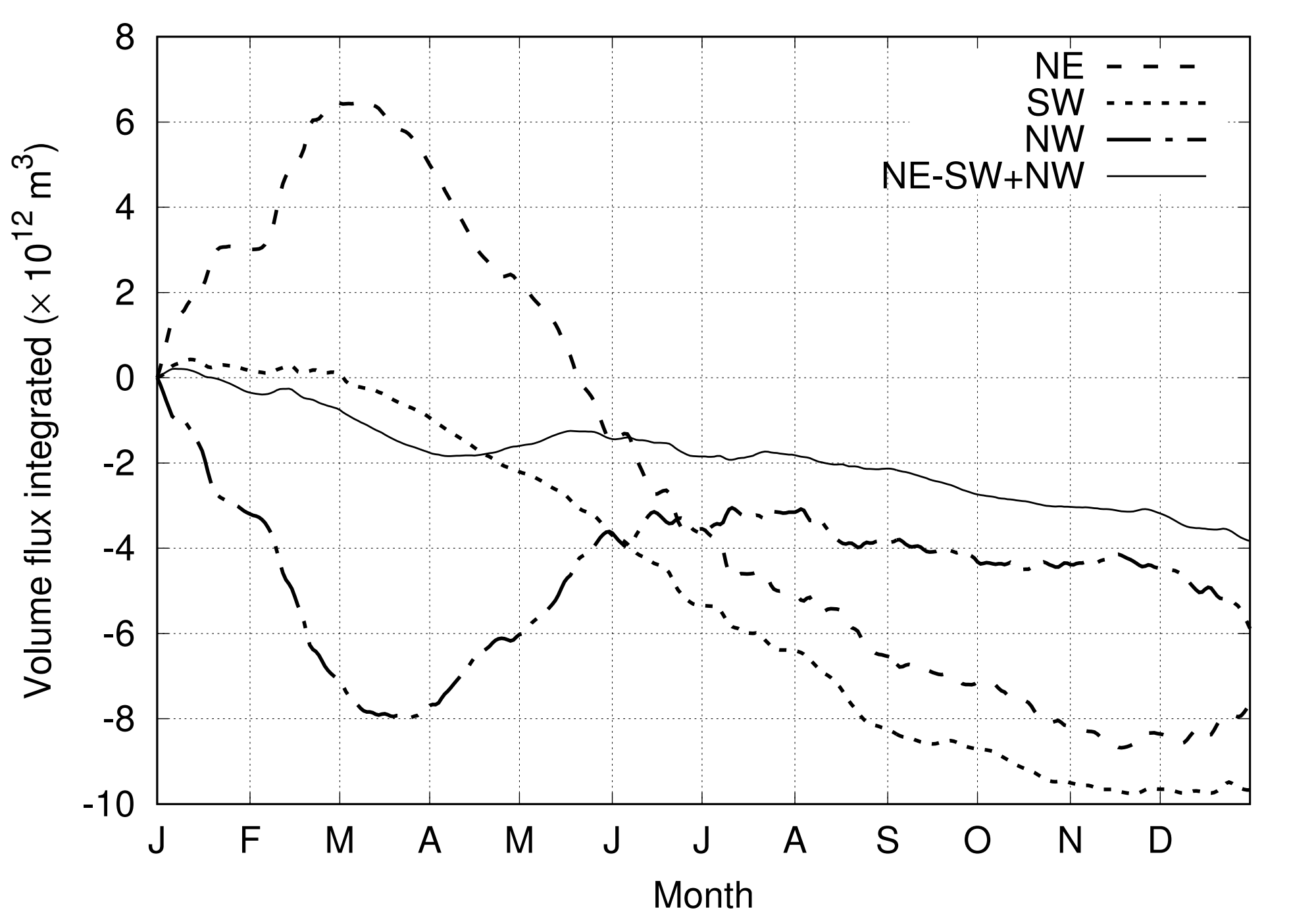
NE
SW
NW
NE-SW+NW
8
6
4
2
0
-2
-4
-6
-8
-10
Volume flux integrated (× 10^12 m^3)
J
F
M
A
M
J
J
A
S
O
N
D
Month

Figure 4.

(a) summer

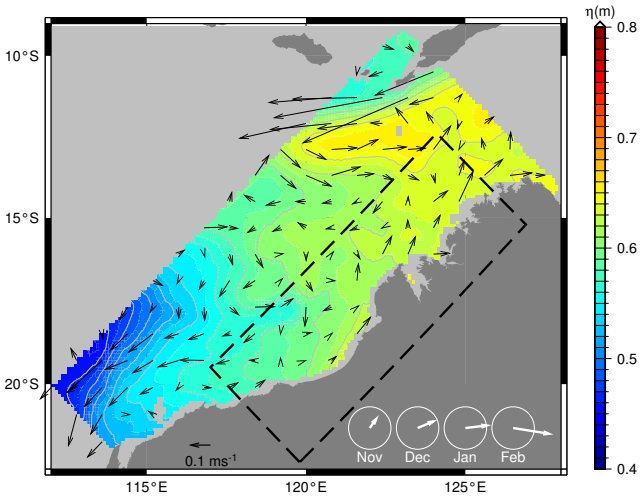

(b) autumn

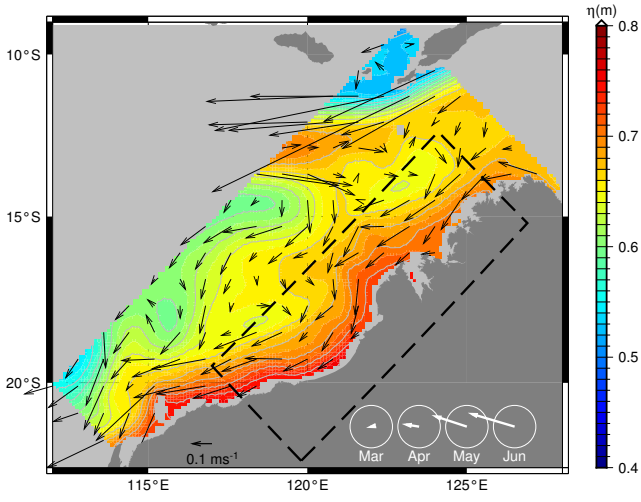

(c) winter/spring

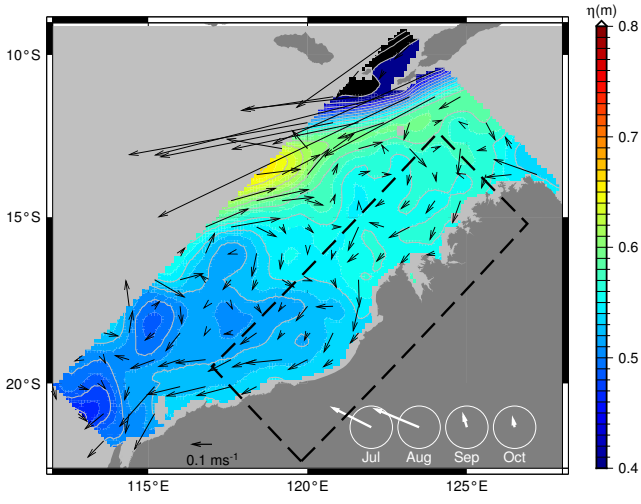

Figure 5.

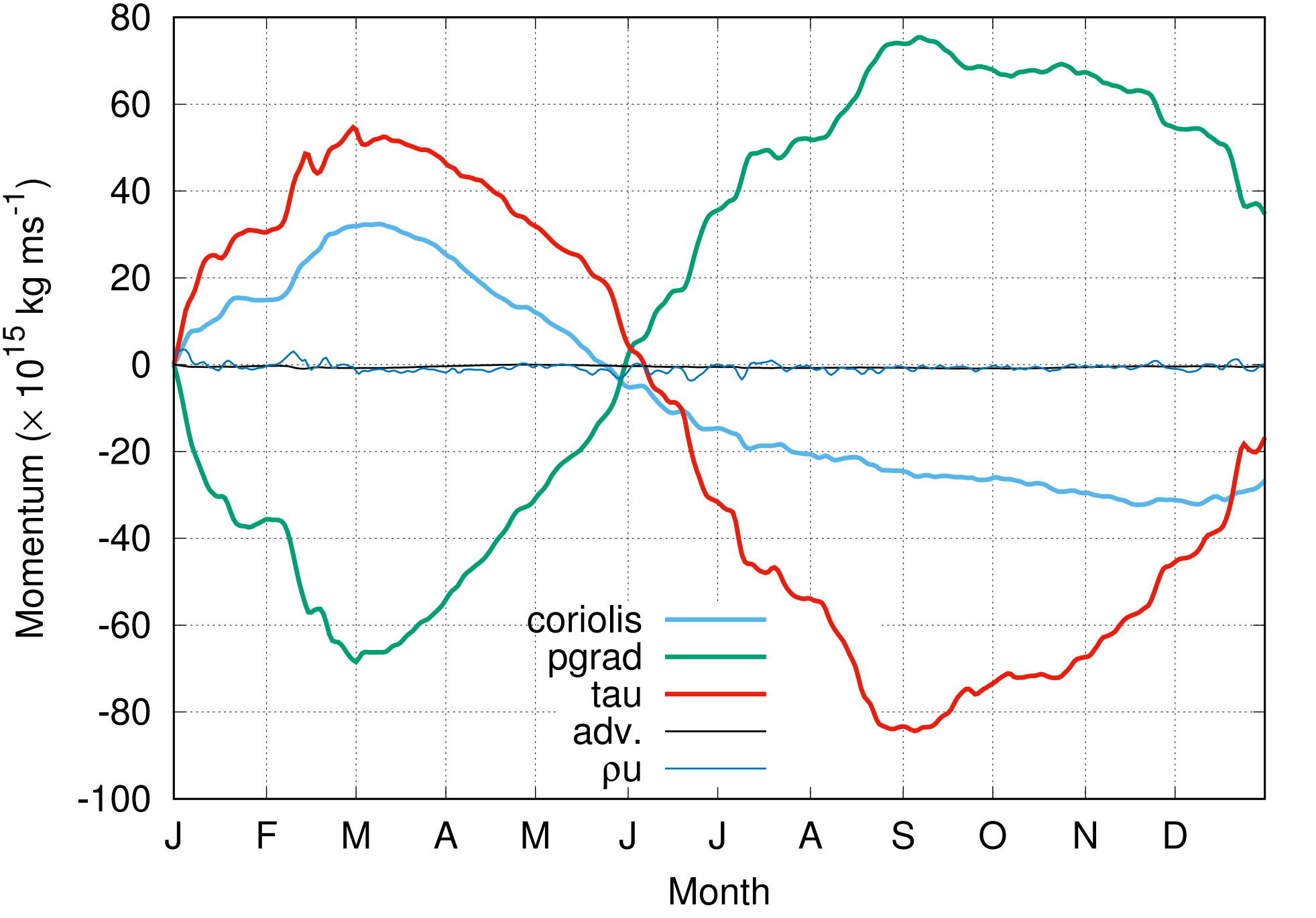
80
60
40
20
0
-20
-40
-60
-80
-100
Momentum (× 10^15 kg ms^-1)
J
F
M
A
M
J
J
A
S
O
N
D
Month
coriolis
pgrad
tau
adv.
ρu

Figure 6.

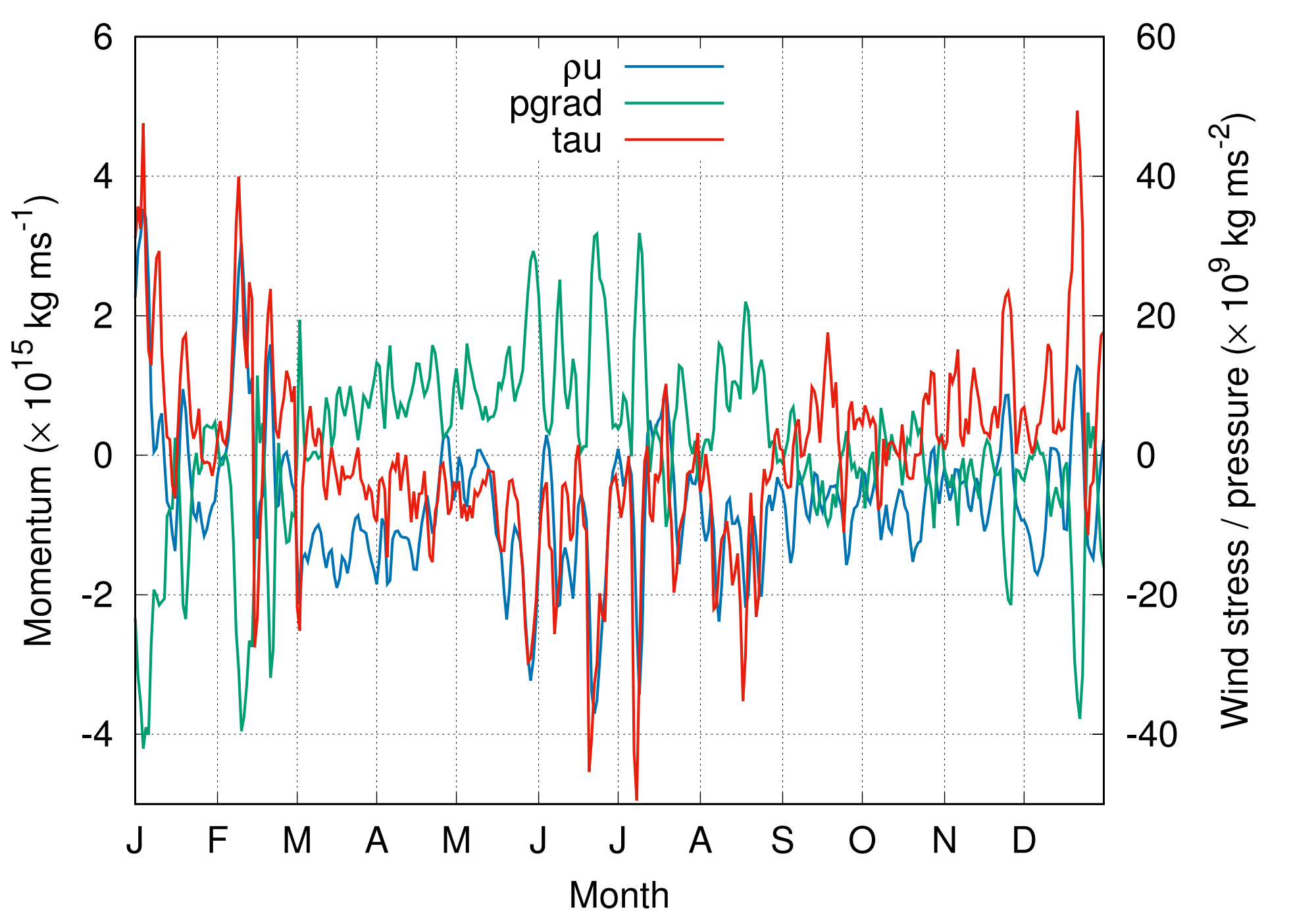
ρu
pgrad
tau
6
4
2
0
-2
-4
60
40
20
0
-20
-40
J
F
M
A
M
J
J
A
S
O
N
D
Month
Momentum (× 10^15 kg ms^-1)
Wind stress / pressure (× 10^9 kg ms^-2)

Figure 7.

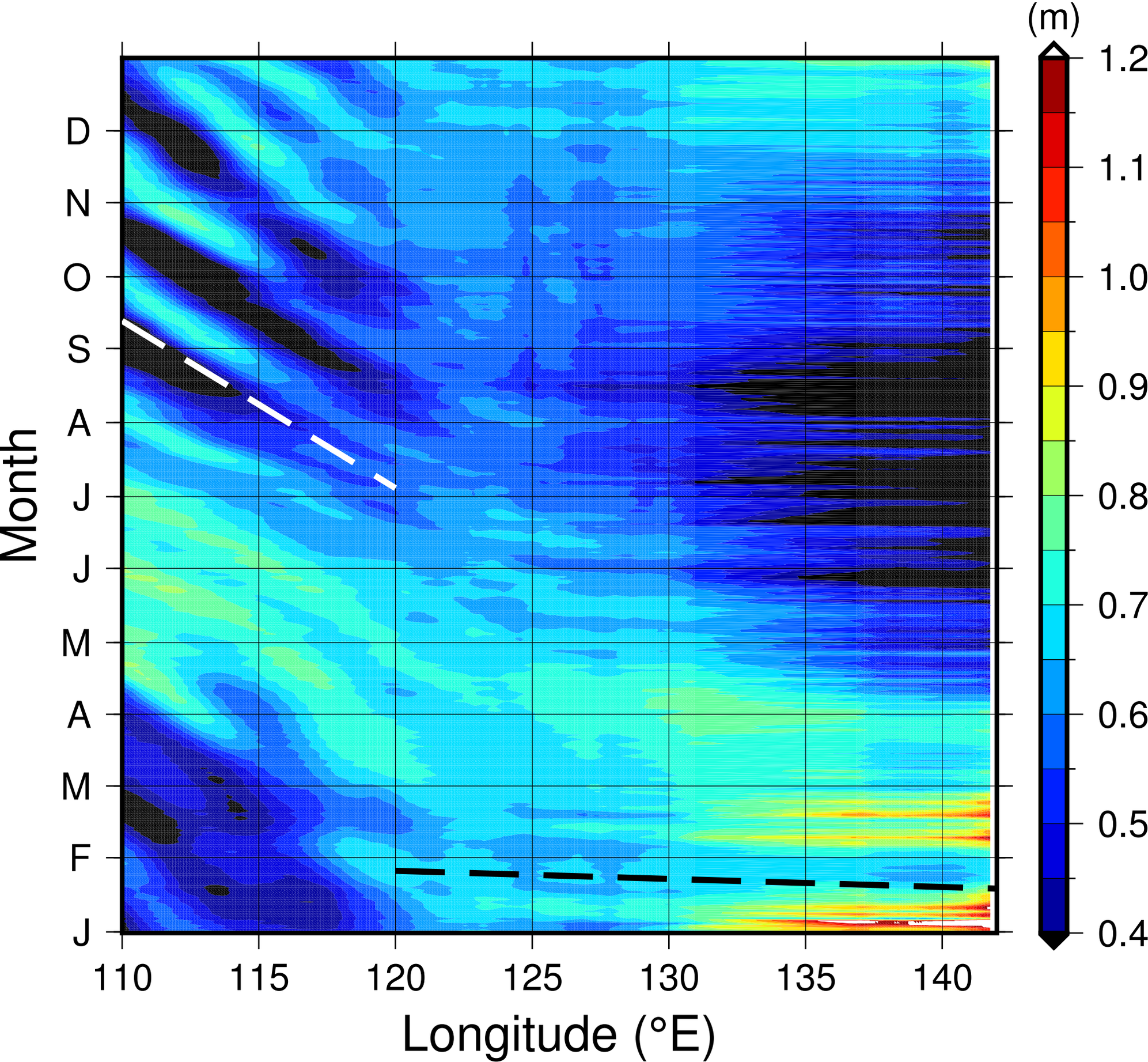
(m)
1.2
1.1
1.0
0.9
0.8
0.7
0.6
0.5
0.4
Month
D
N
O
S
A
J
J
M
A
M
F
J
110
115
120
125
130
135
140
Longitude (°E)

Figure 8.

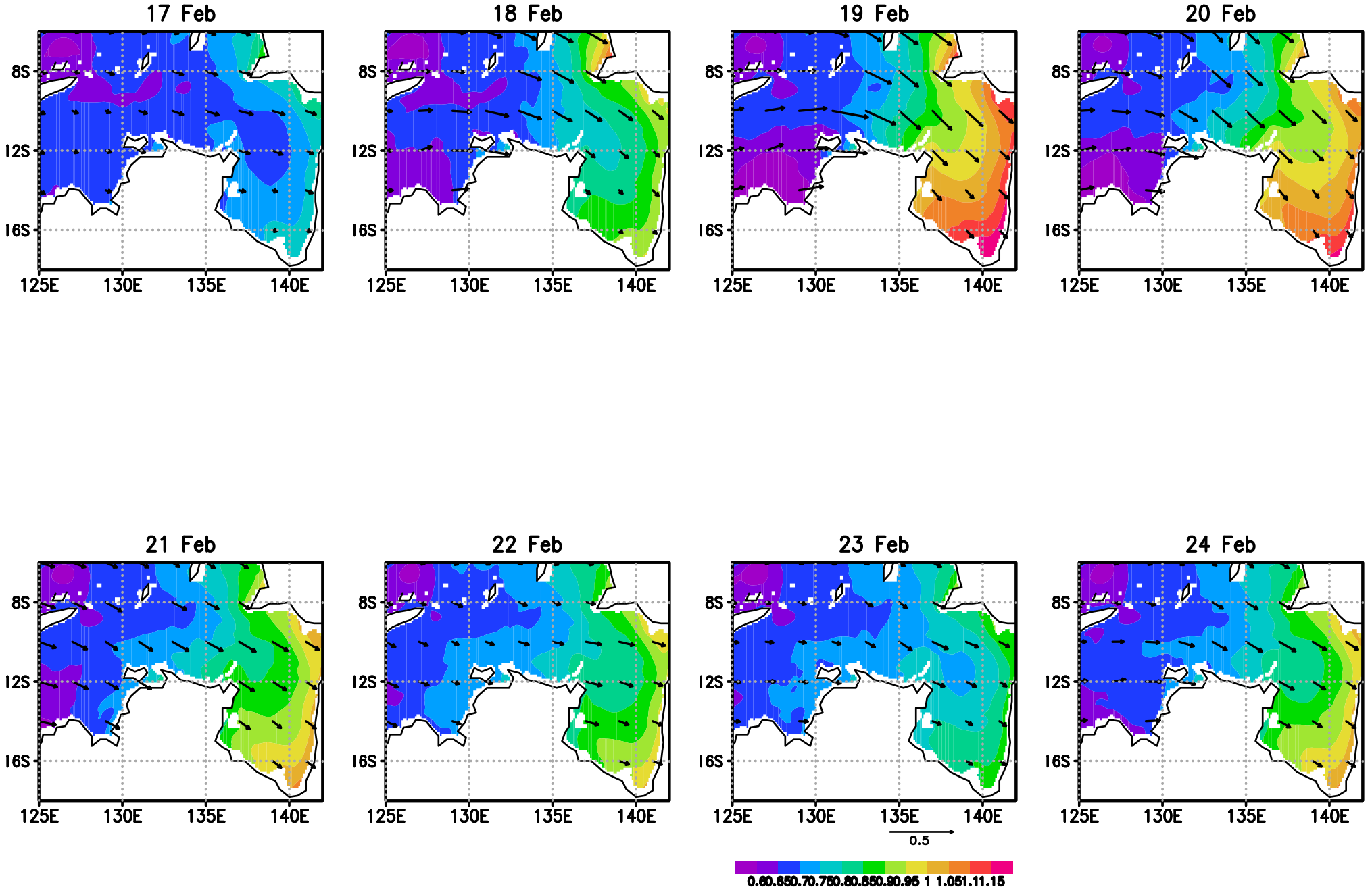
17 Feb
18 Feb
19 Feb
20 Feb
21 Feb
22 Feb
23 Feb
24 Feb
8S
12S
16S
125E
130E
135E
140E
0.5
0.6 0.65 0.7 0.75 0.8 0.85 0.9 0.95 1 1.05 1.1 1.15

Figure 9.

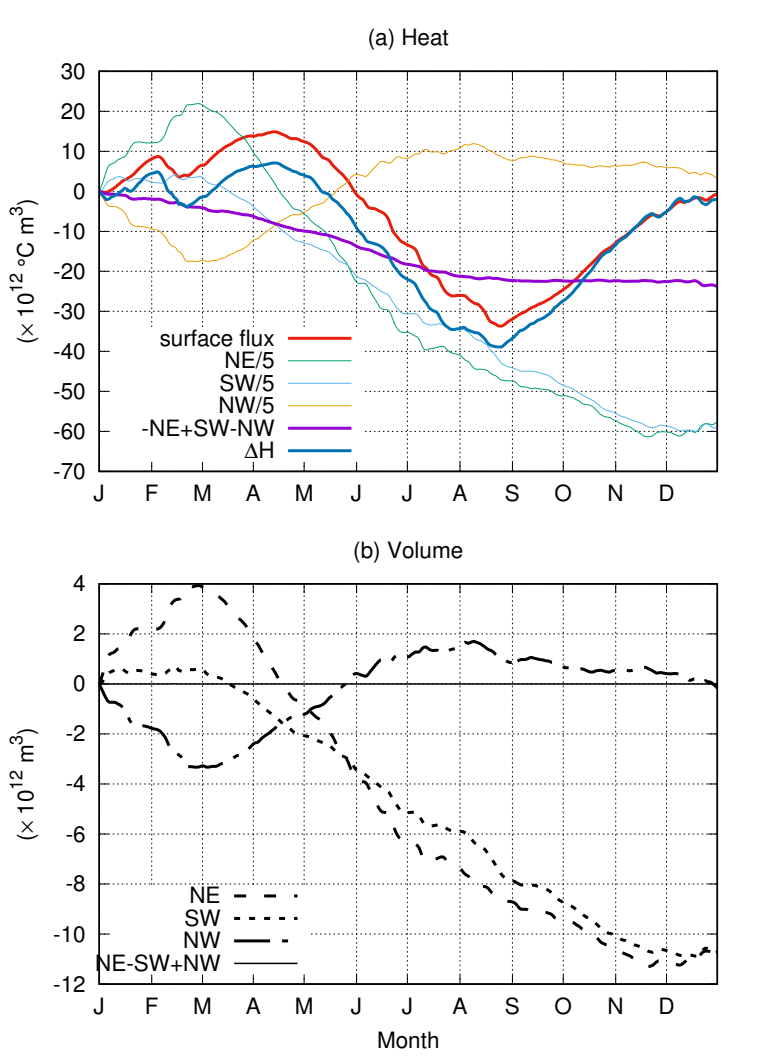
(a) Heat
(× 10^12 °C m^3)
surface flux
NE/5
SW/5
NW/5
-NE+SW-NW
ΔH
J F M A M J J A S O N D
(b) Volume
(× 10^12 m^3)
NE
SW
NW
NE-SW+NW
Month

Figure 10.

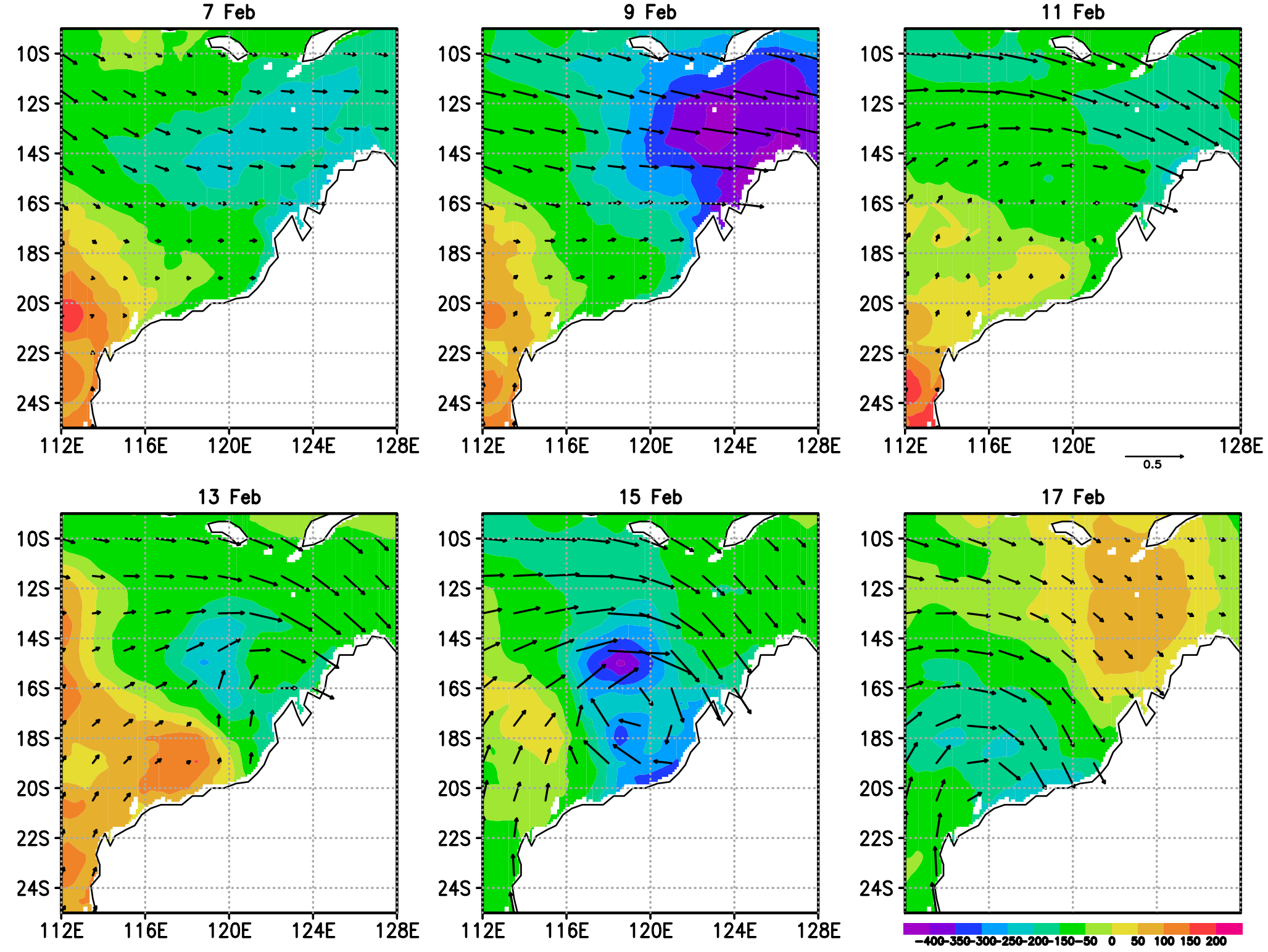
7 Feb
9 Feb
11 Feb
13 Feb
15 Feb
17 Feb
10S
12S
14S
16S
18S
20S
22S
24S
112E
116E
120E
124E
128E
0.5
−400 −350 −300 −250 −200 −150 −50 0 50 100 150 200